INTERNATIONAL JOURNAL FOR NUMERICAL METHODS IN FLUIDS, VOL. 12, 911–928 (1991)

A SOLUTION FOR THE VERTICAL VARIATION OF STRESS, RATHER THAN VELOCITY, IN A THREE-DIMENSIONAL CIRCULATION MODEL

RICHARD A. LUETTICH JR.

University of North Carolina at Chapel Hill, Institute of Marine Sciences, 3407 Arendell St., Morehead City, NC 28557, U.S.A.

AND

JOANNES J. WESTERINK

Department of Civil Engineering, University of Notre Dame, Notre Dame, IN 46556, U.S.A.

SUMMARY

A simple technique is presented that allows a numerical solution to be sought for the vertical variation of shear stress as a substitute for the vertical variation of velocity in a three-dimensional hydrodynamic model. In its most general form the direct stress solution (DSS) method depends only upon the validity of an eddy viscosity relation between the shear stress and the vertical gradient of velocity. The rationale for preferring a numerical solution for shear stress to one for velocity is that shear stress tends to vary more slowly over the vertical than velocity, particularly near boundaries. Consequently, a numerical solution can be obtained much more efficiently for shear stress than for velocity. When needed, the velocity profile can be recovered from the stress profile by solving a one-dimensional integral equation over the vertical. For most practical problems this equation can be solved in closed form.

Comparisons are presented between the DSS technique, the standard velocity solution technique and analytical solutions for wind-driven circulation in an unstratified, closed, rectangular channel governed by the linear equations of motion. In no case was the computational effort required by the velocity solution competitive with the DSS when a physically realistic boundary layer was included.

The DSS technique should be particularly beneficial in numerical models of relatively shallow water bodies in which the bottom and surface boundary layers occupy a significant portion of the water column.

KEY WORDS Direct stress solution Vertical velocity profiles Three-dimensional circulation model Spectral methods

INTRODUCTION

In large part owing to their computational efficiency, two-dimensional, vertically integrated hydrodynamic models have become an important and widely used tool for modelling horizontal circulation in coastal, shelf and even open ocean settings when vertical density stratification can be neglected. Although more sophisticated approaches have been developed for specialized conditions,[1–3] two-dimensional hydrodynamic models are typically limited to representing bottom stress as a collinear function of the depth-averaged velocity and parametrizing the shear dispersion[3] (i.e. the contribution from the vertical variation of horizontal velocity to the depth-averaged convective acceleration terms) as a 'diffusion-like' process. These approximations can be

0271–2091/91/100911–18$09.00

Received 2 May 1990
Revised 31 July 1990

implemented rigorously only when the vertical profile of horizontal velocity can be assumed *a priori*, such as for simple tidal flows.[3] Unfortunately, it is impossible to assume a relation between bottom stress and depth-averaged velocity that is generally valid for flows such as Ekman layers or wind-driven circulation in enclosed or semi-enclosed basins (since the alignment of the depth-averaged velocity differs from that of the bottom stress by an unknown angle), or when wave orbital velocities or suspended sediment concentration gradients are significant near the bottom (since both can contribute to the bottom stress). It is also impossible to assume values for the shear dispersion coefficients for complex flows. Finally, if velocities generated by a two-dimensional hydrodynamic model are used in a transport model, it is impossible to account for variations over the vertical in the magnitude and direction of the advective transport terms in complex flows. For these reasons it is often necessary to use a model that explicitly includes the vertical variation of horizontal velocity.

A significant problem for numerical models that explicitly include the vertical variation of horizontal velocity is the presence of potentially steep vertical velocity gradients near the bottom and free surface boundaries and near sharp density interfaces. To resolve these gradient regions, existing numerical models must use fine discretizations over the vertical (at least locally). Owing to the substantial computational burden that results, the gradient regions are often omitted and their effects on the remainder of the water column approximated by various slip conditions.[4,5] This approach is particularly appropriate in deep water where the depth is large in comparison with the thickness of the boundary layers. However, in coastal and shelf applications the surface and bottom boundary layers occupy a significant portion (if not all) of the water column. Therefore it is preferable to explicitly model the entire water column if this can be done at reasonable cost.

It is well known both theoretically and experimentally that, contrary to velocity, shear stress varies slowly near boundaries.[6-8] Consequently, it should be much more efficient to discretize and solve numerically for the vertical variation of shear stress near a boundary than it is to solve for the vertical variation of velocity. In this paper a technique is presented to solve for the vertical variation of shear stress rather than velocity in a numerical, three-dimensional model of nearly horizontal circulation. An initial demonstration of the usefulness of this direct stress solution (DSS) technique is presented by comparing it with a standard velocity solution (VS) technique and with analytical solutions for steady state, periodic and transient test cases.

FORMULATION

Using a gradient eddy viscosity hypothesis to relate shear stress and horizontal velocity,

$$\frac{\tau_{zx}}{\rho} \equiv \frac{a-b}{H} E_z \frac{\partial U}{\partial \sigma} \quad \text{and} \quad \frac{\tau_{zy}}{\rho} \equiv \frac{a-b}{H} E_z \frac{\partial V}{\partial \sigma}, \tag{1}$$

where, $H(x, y, t) = \eta + h - z_0$ is the water depth from the top of the effective bottom roughness to the free surface, $\eta(x, y, t)$ is the water surface elevation above the still water level, $h(x, y, t)$ is the nominal water depth below the still water level (bathymetric depth), $z_0(x, y, t)$ is the zero-velocity height or effective bottom roughness height, $\sigma \equiv a + (a-b)(z-\eta)/H$ is a stretched vertical co-ordinate where $\sigma = b$ at the top of the effective bottom roughness and $\sigma = a$ at the free surface,[9] $\tau_{zx}(x, y, z, t)$ and $\tau_{zy}(x, y, z, t)$ are vertical shear stresses in the x- and y-directions, $U(x, y, z, t)$ and $V(x, y, z, t)$ are horizontal velocities in the x- and y-directions, $E_z(x, y, z, t)$ is the vertical eddy viscosity, $\rho(x, y, z, t)$ is the density of water, x and y are the two horizontal co-ordinates, z is the vertical co-ordinate, positive upward with $z = 0$ at the still water level, and t is time.

The gradient eddy viscosity hypothesis has been particularly successful in modelling boundary-layer-type flows[2,10] and is therefore consistent with the purpose of the DSS, i.e. to model flows in which boundary layers occupy a significant portion of the water column. We note that E_z may vary in the three spatial dimensions and/or time and may be specified directly or computed by using higher-order equations for turbulent kinetic energy, dissipation and/or mixing length.[11]

Integrating equation (1) from the top of the effective bottom roughness upwards gives expressions for the horizontal velocity:

$$U(\sigma)=U_b+\frac{H}{a-b}\int_b^\sigma \frac{\tau_{zx}}{\rho E_z}\,d\sigma \quad \text{and} \quad V(\sigma)=V_b+\frac{H}{a-b}\int_b^\sigma \frac{\tau_{zy}}{\rho E_z}\,d\sigma. \tag{2}$$

Although physically unrealistic, non-zero bottom slip velocities U_b and V_b have been included in equation (2) for generality. Relating U_b and V_b to the bottom stresses τ_{bx} and τ_{by} via a linear slip boundary condition yields

$$\tau_{bx}/\rho=kU_b \quad \text{and} \quad \tau_{by}/\rho=kV_b, \tag{3}$$

where k is the dimensional (length/time) linear slip coefficient. Substituting equation (3) in equation (2) gives expressions for the horizontal velocity that are entirely in terms of stress:

$$U(\sigma)=\frac{\tau_{bx}}{\rho k}+\frac{H}{a-b}\int_b^\sigma \frac{\tau_{zx}}{\rho E_z}\,d\sigma \quad \text{and} \quad V(\sigma)=\frac{\tau_{bx}}{\rho k}+\frac{H}{a-b}\int_b^\sigma \frac{\tau_{zy}}{\rho E_z}\,d\sigma. \tag{4}$$

(For a no-slip boundary condition the terms $\tau_{bx}/\rho k$ and $\tau_{by}/\rho k$ do not appear in equation (4). The no-slip condition is approached as $k\to\infty$.)

If equation (4) is substituted in the equations of motion describing nearly horizontal flow (e.g. equations (10)–(12)[9]), velocity can be eliminated and an equation set obtained solely in terms of shear stress and water surface elevation. Alternatively, equation (4) can be used to eliminate velocity only from equations for the vertical variation of momentum. (These equations are derived by subtracting the depth-averaged momentum equations from the full momentum equations.) If this is done, the depth-averaged continuity and momentum equations can be solved in standard form,[12,13] with the exception that τ_b and the shear dispersion terms are no longer parametrized in terms of $\bar{U}$, $\bar{V}$ but rather are computed from the results of the DSS for the vertical variation of momentum.

In the present paper the application and merit of the DSS technique are demonstrated using the linearized equations governing unstratified, nearly horizontal flow with negligible Coriolis force:

$$\frac{\partial\eta}{\partial t}+h\frac{\partial\bar{U}}{\partial x}=0, \tag{5}$$

$$\frac{\partial\bar{U}}{\partial t}=-g\frac{\partial\eta}{\partial x}+\frac{1}{h\rho}(\tau_s-\tau_b), \tag{6}$$

$$\frac{\partial u}{\partial t}-\frac{a-b}{h}\frac{\partial}{\partial\sigma}\left(\frac{\tau_z}{\rho}\right)=\frac{1}{h\rho}(\tau_b-\tau_s), \tag{7}$$

where, g is the acceleration due to gravity, $\tau_s(x, y, t)$ is the shear stress at the free surface, $\tau_b(x, y, t)$ is the shear stress at the bottom, $\bar{U}(x, y, t)$ is the depth-averaged velocity, defined as $\bar{U}\equiv[1/(a-b)]\int_b^a U\,d\sigma$, and $u(x, y, \sigma, t)$ is the velocity departure from depth average, defined as $u\equiv U-\bar{U}$. Equation (5) is the depth-integrated continuity equation, equation (6) is the depth-integrated momentum equation and equation (7) expresses the vertical variation of momentum.

These equations retain most of the vertical physics present in the full equation set and, for a time-invariant value of E_z, can be solved analytically in both the horizontal and vertical direction. By neglecting the Coriolis force, the equations of motion are uncoupled in the two horizontal directions. Therefore only motion aligned with the x-direction is considered. However, as discussed below, the efficiency of the DSS technique for the more general case of a non-zero Coriolis force can be demonstrated using these results.

Substituting equation (4) in equation (7) to eliminate u yields

$$\frac{h}{a-b}\frac{\partial}{\partial t}\int_b^\sigma \frac{\tau_z}{\rho E_z}\,d\sigma + \frac{1}{k}\frac{\partial}{\partial t}\left(\frac{\tau_b}{\rho}\right) - \frac{\tau_b}{h\rho} - \frac{a-b}{h}\frac{\partial}{\partial \sigma}\left(\frac{\tau_z}{\rho}\right) = \frac{\partial \bar{U}}{\partial t} - \frac{\tau_s}{h\rho}. \tag{8}$$

(To be consistent with the linearization of the governing equations, it has been assumed that $h \approx H$ in equation (4).)

Equation (8) contains both integral and differential terms; therefore it is particularly well suited for a spatial discretization in which τ_z is expressed in terms of assumed shape functions, such as in the spectral or finite element methods. Depending on the choice of these shape functions and the functional variation of E_z over the depth, the velocity profile can be recovered from the stress profile by solving equation (4) *in closed form*. This is an important convenience because it avoids the troublesome operation of numerically integrating the near-logarithmic singularity that occurs in equation (4) when E_z varies with distance from a boundary. The restrictions that a closed-form solution for equation (4) imposes on τ_z and E_z are not severe. For example, both τ_z and E_z may be expressed by polynomials that span the vertical either globally or in a piecewise manner. A polynomial variation of τ_z is consistent with either a spectral or a finite element discretization of equation (8); for most practical problems E_z can be approximated as being piecewise linear over the vertical.[2,9,14]

In the test cases presented below, the Galerkin–spectral method, with shape functions consisting of Legendre polynomials (LPs) over the interval $-1 \leqslant \sigma \leqslant 1$, is used to discretize the VS (equation (7)) and the DSS (equation (8)). It has been shown for wind-driven circulation that velocity solutions using Legendre and Chebyshev polynomials yield solutions of virtually identical accuracy, that these are highly superior to velocity solutions obtained using expansions of trigonometric functions and that these are more accurate than velocity solutions computed with a second-order finite difference scheme having the same number of degrees of freedom.[15,16] For further information on the use of spectral methods in three-dimensional circulation models, the interested reader is referred to an excellent review by Davies.[9]

The Galerkin–spectral discretization for the VS is obtained by multiplying equation (7) by the weighting function $\phi_m(\sigma)$ and integrating from -1 to 1, i.e.

$$\frac{\partial}{\partial t}\int_{-1}^{1}\phi_m(\sigma)u\,d\sigma - \frac{2}{h}\int_{-1}^{1}\phi_m(\sigma)\frac{\partial}{\partial \sigma}\left(\frac{\tau_z}{\rho}\right)d\sigma = -\frac{1}{h}\left(\frac{\tau_s}{\rho}-\frac{\tau_b}{\rho}\right)\int_{-1}^{1}\phi_m(\sigma)\,d\sigma. \tag{9}$$

Integrating the stress derivative term in equation (9) by parts gives

$$\frac{2}{h}\int_{-1}^{1}\phi_m(\sigma)\frac{\partial}{\partial \sigma}\left(\frac{\tau_z}{\rho}\right)d\sigma = \frac{2}{h}\left[\phi_m(1)\frac{\tau_s}{\rho} - \phi_m(-1)\frac{\tau_b}{\rho} - \int_{-1}^{1}\frac{\tau_z}{\rho}\frac{\partial \phi_m(\sigma)}{\partial \sigma}\,d\sigma\right] \tag{10}$$

and substituting this in equation (9) yields

$$\frac{\partial}{\partial t}\int_{-1}^{1}\phi_m(\sigma)\,u\,d\sigma + \frac{2}{h}\int_{-1}^{1}\frac{\tau_z}{\rho}\frac{\partial \phi_m(\sigma)}{\partial \sigma}\,d\sigma = -\frac{1}{h}\left[\frac{\tau_s}{\rho}-\frac{\tau_b}{\rho}\right]\int_{-1}^{1}\phi_m(\sigma)\,d\sigma + \frac{2}{h}\left[\phi_m(1)\frac{\tau_s}{\rho} - \phi_m(-1)\frac{\tau_b}{\rho}\right]. \tag{11}$$

Using the definition of the LPs (Table I), equation (11) simplifies to

$$m=0: \quad 0=0, \tag{12}$$

$$m\geqslant 1: \quad \frac{\partial}{\partial t}\int_{-1}^{1}\phi_m(\sigma)u\,\mathrm{d}\sigma+\frac{2}{h}\int_{-1}^{1}\frac{\tau_z}{\rho}\frac{\partial\phi_m(\sigma)}{\partial\sigma}\,\mathrm{d}\sigma=\frac{2}{h}\left[\frac{\tau_s}{\rho}-\phi_m(-1)\frac{\tau_b}{\rho}\right]. \tag{13}$$

Since $\phi_0(\sigma)=1$, the operation that generates equation (11) is equivalent to integrating equation (7) over the depth when $m=0$. The identity in equation (12) occurs because equation (7), by definition, has no depth-averaged component.

Table I. Galerkin–spectral equations

Legendre polynomials

$\phi_0(\sigma)=1,$

$\phi_1(\sigma)=\sigma,$

$$\phi_{r+1}(\sigma)=\left[\frac{2r+1}{r+1}\right]\sigma\phi_r-\left[\frac{r}{r+1}\right]\phi_{r-1},$$

$\phi_r(1)=1,$

$$\int_{-1}^{1}\phi_0(\sigma)\,\mathrm{d}\sigma=2,$$

$$\int_{-1}^{1}\phi_r(\sigma)\,\mathrm{d}\sigma=0 \text{ for } r\geqslant 1.$$

Velocity expansion

$$u(\sigma,t)\equiv\sum_{n=1}^{N}\beta_n(t)\phi_n(\sigma), \tag{14}$$

$$m\geqslant 1: \quad \frac{h^2}{4}\sum_{n=1}^{N}\frac{\partial\beta_n(t)}{\partial t}\int_{-1}^{1}\phi_m(\sigma)\phi_n(\sigma)\,\mathrm{d}\sigma+\sum_{n=1}^{N}\beta_n(t)\int_{-1}^{1}E_z(\sigma)\frac{\partial\phi_n(\sigma)}{\partial\sigma}\frac{\partial\phi_m(\sigma)}{\partial\sigma}\,\mathrm{d}\sigma$$
$$=\frac{h}{2}\left[\frac{\tau_s(t)}{\rho}-\frac{\tau_b(t)}{\rho}\phi_m(-1)\right], \tag{15}$$

$$\sum_{n=1}^{N}\beta_n(t)\phi_n(-1)=-\bar{U}(t)+\frac{\tau_b(t)}{k\rho}. \tag{16}$$

Stress expansion

$$\frac{\tau_z(\sigma,t)}{\rho}\equiv\sum_{n=0}^{N}\alpha_n(t)\phi_n(\sigma), \tag{21}$$

$$m\geqslant 1: \quad \frac{h^2}{4}\sum_{n=0}^{N}\frac{\partial\alpha_n(t)}{\partial t}\int_{-1}^{1}\phi_m(\sigma)\int_{-1}^{\sigma}\frac{\phi_n(\sigma)}{E_z(\sigma)}\,\mathrm{d}\sigma\,\mathrm{d}\sigma$$
$$+\sum_{n=0}^{N}\alpha_n(t)\left[\int_{-1}^{1}\phi_n(\sigma)\frac{\partial\phi_m(\sigma)}{\partial\sigma}\,\mathrm{d}\sigma+\phi_n(-1)\phi_m(-1)\right]=\frac{\tau_s(t)}{\rho}, \tag{22}$$

$$\sum_{n=0}^{N}\alpha_n(t)\left[\frac{\phi_n(-1)}{kh}+\frac{1}{4}\int_{-1}^{1}\int_{-1}^{\sigma}\frac{\phi_n(\sigma)}{E_z(\sigma)}\,\mathrm{d}\sigma\,\mathrm{d}\sigma\right]=\frac{\bar{U}(t)}{h}. \tag{24}$$

The final steps in applying the Galerkin–spectral method to the VS are to substitute equation (1) for τ_z/ρ in equation (13) (noting that $\partial U/\partial\sigma = \partial u/\partial\sigma$) and expand u as a series of LPs (Table I, equation (14)). The result is given by eqution (15) in Table I. Because $\int_{-1}^{1} \phi_n(\sigma)\,d\sigma = 0$ for $n \geqslant 1$, by using only the $n \geqslant 1$ LPs the condition $\int_{-1}^{1} u\,d\sigma = 0$ is identically satisfied by the spectral solution. Equation (15) must be solved with the bottom boundary condition (equation (3)). After expanding u, this is expressed by equation (16) in Table I.

The Galerkin–spectral discretization for the DSS is obtained by multiplying equation (8) by the weighting function $\phi_m(\sigma)$ and integrating from -1 to 1, i.e.

$$\frac{h}{2}\frac{\partial}{\partial t}\left[\int_{-1}^{1}\phi_m(\sigma)\int_{-1}^{\sigma}\frac{\tau_z}{\rho E_z}\,d\sigma\,d\sigma\right]+\left[\frac{1}{k}\frac{\partial}{\partial t}\left(\frac{\tau_b}{\rho}\right)-\frac{\tau_b}{h\rho}\right]\int_{-1}^{1}\phi_m(\sigma)\,d\sigma-\frac{2}{h}\int_{-1}^{1}\phi_m(\sigma)\frac{\partial}{\partial\sigma}\left(\frac{\tau_z}{\rho}\right)d\sigma$$
$$=\left[\frac{\partial\bar{U}}{\partial t}-\frac{\tau_s}{h\rho}\right]\int_{-1}^{1}\phi_m(\sigma)\,d\sigma. \tag{17}$$

Integrating the stress derivative by parts changes equation (17) to

$$\frac{h}{2}\frac{\partial}{\partial t}\left[\int_{-1}^{1}\phi_m(\sigma)\int_{-1}^{\sigma}\frac{\tau_z}{\rho E_z}\,d\sigma\,d\sigma\right]+\left[\frac{1}{k}\frac{\partial}{\partial t}\left(\frac{\tau_b}{\rho}\right)-\frac{\tau_b}{h\rho}\right]\int_{-1}^{1}\phi_m(\sigma)\,d\sigma$$
$$-\frac{2}{h}\left[\phi_m(1)\frac{\tau_s}{\rho}-\phi_m(-1)\frac{\tau_b}{\rho}-\int_{-1}^{1}\frac{\tau_z}{\rho}\frac{\partial\phi_m(\sigma)}{\partial\sigma}\,d\sigma\right]=\left[\frac{\partial\bar{U}}{\partial t}-\frac{\tau_s}{h\rho}\right]\int_{-1}^{1}\phi_m(\sigma)\,d\sigma. \tag{18}$$

Using the definition of the LPs (Table I), equation (18) simplifies to

$$m=0:\quad 0=0 \tag{19}$$

$$m\geqslant 1:\quad \frac{h}{2}\frac{\partial}{\partial t}\left[\int_{-1}^{1}\phi_m(\sigma)\int_{-1}^{\sigma}\frac{\tau_z}{\rho E_z}\,d\sigma\,d\sigma\right]+\frac{2}{h}\left[\phi_m(-1)\frac{\tau_b}{\rho}+\int_{-1}^{1}\frac{\tau_z}{\rho}\frac{\partial\phi_m(\sigma)}{\partial\sigma}\,d\sigma\right]=2\frac{\tau_s}{h\rho}. \tag{20}$$

The identity in equation (19) occurs because equation (8) has no depth-averaged component.

The final step in applying the Galerkin–spectral method for the DSS is to expand τ_z/ρ as a series of LPs (Table I, equation (21)). The result is given by equation (22) in Table I. The bottom boundary condition was introduced into equation (4) and subsequently into equation (8). Therefore it does not generate an extra equation as was the case for the VS. However, the stress expansion in equation (21) does not automatically satisfy the condition $\int_{-1}^{1} u\,d\sigma = 0$; rather, this must be enforced explicitly. Using equation (4) and the definition of U, this requirement generates the additional equation

$$\int_{-1}^{1}\left[-\bar{U}+\frac{\tau_b}{\rho k}+\frac{h}{2}\int_{-1}^{\sigma}\frac{\tau_z}{\rho E_z}\,d\sigma\right]d\sigma=0. \tag{23}$$

Substituting the expansion for τ_z/ρ in equation (23) yields equation (24) in Table I.

The Galerkin–spectral method using polynomial bases yields fully populated matricies.[15] Therefore, for the general problem, the computational effort required to set up, decompose and solve for the spectral coefficients in both the VS and the DSS scales with N^3, where N is the number of LPs used in each solution. If E_z is constant in time, it is necessary to set up and decompose the matrices only at the first time step. Subsequently, only forward and backward substitution are required and the computations scale as N^2. When the DSS technique is used, N^2 additional operations are required to evaluate the velocity at any elevation using the closed-form solution to equation (4). Similarly, N^2 operations are required to explicitly evaluate the shear dispersion terms. If the solution over the vertical is to be used only to provide bottom stress for a

two-dimensional hydrodynamic model,[5] it is never necessary to explicitly determine the velocity profile and these additional operations are not required.

TEST CASES

The relative merit of the DSS versus the VS was evaluated by comparing solutions computed numerically with analytical solutions for the problem of wind-driven circulation in a closed, rectangular channel aligned with the x-axis and having a constant bathymetric depth. This was done for a steady state case, for a periodically varying wind stress and for an instantaneously imposed wind stress.

In each test case E_z was assumed to be linear over the depth as expressed by

$$E_z(\sigma) = E_{z0}(\sigma + 1 + \sigma_0), \tag{25}$$

where $\sigma_0 \equiv 2z_0/h$ is the dimensionless roughness height. It is well known from theoretical, laboratory and field experiments that an eddy viscosity that increases linearly with distance from a solid boundary realistically reproduces the physics of the boundary layer near the boundary.[6-8] Despite the fact that this does not hold over the entire depth (e.g., it has been suggested that E_z should also increase linearly with distance below the free surface[2]), equation (25) is used here because it generates a realistic bottom boundary layer and because it simplifies the analyses of model results by introducing only two parameters, E_{z0} and σ_0, into the problem. As is shown below, the presence of a velocity gradient region at the bottom is sufficient to illustrate the advantage of the DSS over the VS. In fact, the use of an eddy viscosity that does not also give a boundary layer at the free surface is a considerable advantage for the VS since it eliminates the additional need to reproduce velocity gradients there.

Assuming reasonable ranges for z_0 of 0·1–10 cm and for h of 1–100 m suggests values of $\sigma_0 \sim 10^{-5}$–10^{-2} in equation (25). (The combination of $z_0 = 10$ cm and $h = 1$ m, which gives $\sigma_0 \sim 10^{-1}$, is not considered realistic since z_0 is typically 3%–10% of the physical roughness height. In this case the physical roughness would occupy the entire depth.) Assuming the slope of the variation of E_z with z scales with U_b^* ($U_b^* \equiv \sqrt{(\tau_b/\rho)}$), then $E_{z0} \sim U_b^* h$. If U_b^* varies over the range 0·1–10 cm s^{-1}, then $E_{z0} \sim 10^{-3}$–10 m^2 s^{-1}.

Table I shows that the VS and DSS require the specification of τ_s/ρ (which is the input forcing) and $\bar{U}$. To eliminate the possibility that errors in the solution for $\bar{U}$ might affect the comparisons, $\bar{U}$ was obtained for each test case from an analytical solution of equations (1), (3) and (5)–(7). A consequence of this procedure is that errors in the VS and DSS over the vertical do not feed back into the solution for $\bar{U}$ as they would if the complete problem was solved numerically.

In all of the results presented below, bottom stresses are obtained from the VS by using computed bottom slip velocities and the linear slip boundary condition (equation (3)). Comparisons indicated that this method gave more accurate values of bottom stress than those obtained by evaluating equation (1) at $\sigma = b$. (A similar conclusion was reached by Gresho *et al.*[17]) Velocities are obtained from the DSS by solving equation (4) analytically using the computed stress profiles.

Steady state

At steady state, equation (7) reduces to

$$\frac{\partial \tau_z}{\partial \sigma} = \frac{\tau_s - \tau_b}{2}, \tag{26}$$

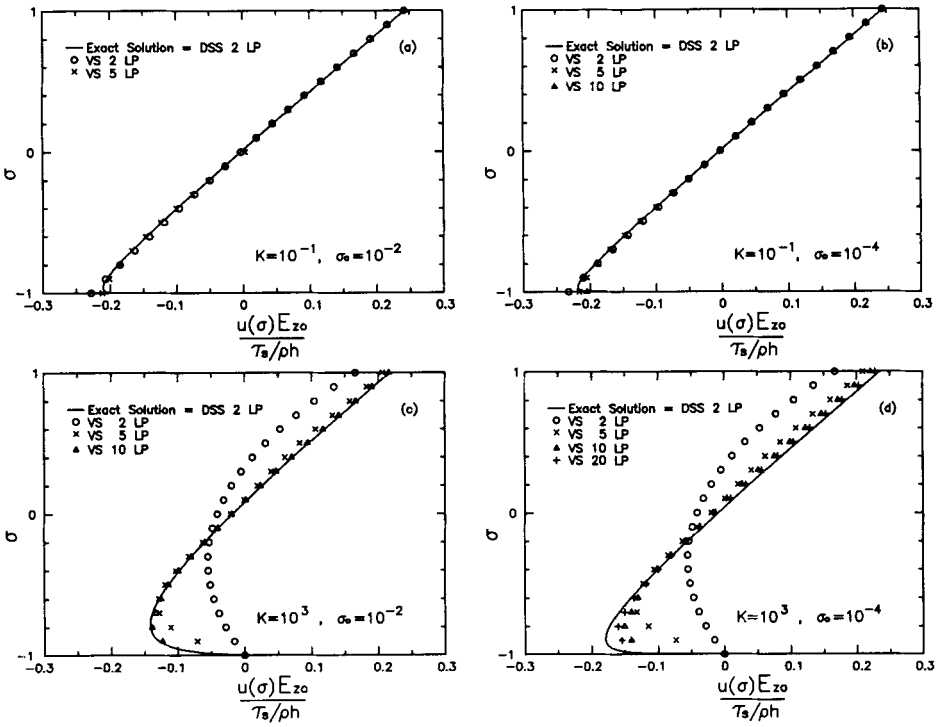

Figure 1. Vertical profiles of horizontal velocity for the steady state test case

which has the analytical solution

$$\frac{\tau_z(\sigma)}{\tau_s} = \frac{\sigma+1}{2} + \frac{1-\sigma}{2}\left(\frac{\tau_b}{\tau_s}\right), \tag{27}$$

where

$$\frac{\tau_b}{\tau_s} = \frac{\left\{-1+\sigma_0\left[\dfrac{2+\sigma_0}{2}\ln\left(\dfrac{2+\sigma_0}{\sigma_0}\right)-1\right]\right\}}{\left\{\dfrac{4}{K}-1+(2+\sigma_0)\left[\dfrac{2+\sigma_0}{2}\ln\left(\dfrac{2+\sigma_0}{\sigma_0}\right)-1\right]\right\}} \tag{28}$$

and $K \equiv kh/E_{z0}$ is the non-dimensional slip coefficient. The non-dimensional solutions for velocity are

$$\frac{\bar{U}E_{z0}}{h\tau_s/\rho} = 0, \tag{29}$$

$$\frac{u(\sigma)E_{z0}}{h\tau_s/\rho} = \frac{\tau_b}{\tau_s}\left[\frac{1}{K} - \frac{\sigma+1}{4} + \frac{2+\sigma_0}{4}\ln\left(\frac{\sigma+1+\sigma_0}{\sigma_0}\right)\right] + \frac{\sigma+1}{4} - \frac{\sigma_0}{4}\ln\left(\frac{\sigma+1+\sigma_0}{\sigma_0}\right). \tag{30}$$

The VS and DSS are obtained from the equations in Table I by dropping the time derivatives, setting $\bar{U}=0$ and considering all other terms to be constant in time.

Figure 1 presents a comparison of vertical profiles of horizontal velocity for several combinations of K and σ_0 computed from the analytical solution, the DSS using two LPs and the VS using

various numbers of LPs. Equation (27) indicates that the analytical solution for stress varies linearly over the depth regardless of the form of E_z. This solution can be represented exactly by the DSS using only the $n=0$ and $n=1$ LPs; therefore the DSS and the analytical solution in Figure 1 are identical. Equation (30) indicates that the analytical solution for velocity has a logarithmic variation over the depth and consequently a potentially sharp gradient region near the bottom. In Figure 1(a) the combination of a small K (large amount of slip) and a large σ_0 minimizes the gradient region. Over most of the depth the velocity profile is nearly linear and therefore closely reproduced using a VS with two LPs. However, approximately five LPs are required to capture the mild velocity gradient near the bed. In Figure 1(b) the same K is used with σ_0 reduced by two orders of magnitude. This has the effect of pushing the gradient region closer to the bottom (i.e. it is equivalent to increasing the depth by a factor of 100 for the same roughness) and therefore steepening the velocity gradient. Because the velocity profile is nearly linear over much of the depth, it is reproduced well by the VS with two LPs. However, near the bed approximately 10 LPs are required for the VS to capture the gradient region. As discussed below, this results in a poor prediction of bottom stress.

In Figures 1(c) and 1(d) a high value of K is used, resulting in essentially no slip at the bottom. For large σ_0 (Figure 1(c)) a velocity expansion of 10 or more LPs is required to reproduce this profile. Reducing σ_0 by two orders of magnitude (Figure 1(d)) sharpens the profile further and approximately 20 LPs are required to capture the velocity profile away from the boundary. Many more are required to represent the gradient region near the boundary.

Table II. Steady state bottom stresses computed using velocity expansions

σ_0	K	No. of LPs	$\left\lvert\frac{\tau_{b(anal)}-\tau_{b(comp)}}{\tau_{b(anal)}}\right\rvert$
10^{-2}	10^{-1}	3	0·100
10^{-2}	1	8	0·091
10^{-2}	10	9	0·099
10^{-2}	10^{2}	10	0·078
10^{-2}	10^{3}	10	0·078
10^{-3}	10^{-1}	8	0·096
10^{-3}	1	21	0·098
10^{-3}	10	24	0·095
10^{-3}	10^{2}	24	0·098
10^{-3}	10^{3}	24	0·099
10^{-4}	10^{-1}	22	0·100
10^{-4}	1	$\leqslant 40$	0·192*
10^{-4}	10	$\leqslant 40$	0·242*
10^{-4}	10^{2}	$\leqslant 40$	0·249*
10^{-4}	10^{3}	$\leqslant 40$	0·249*
10^{-5}	10^{-1}	$\leqslant 40$	0·174*
10^{-5}	1	$\leqslant 40$	0·476*
10^{-5}	10	$\leqslant 40$	0·602*
10^{-5}	10^{2}	$\leqslant 40$	0·619*
10^{-5}	10^{3}	$\leqslant 40$	0·620*

* This is the minimum difference obtained using no more than 40 Legendre polynomials.

As noted above, an important reason for using a three-dimensional model in place of a two-dimensional model is the former's improved representation of the bottom stress. However, since stress is proportional to the velocity gradient (equation (1)), the bottom stress may still be represented poorly if the gradient region near the bottom is not resolved properly in a three-dimensional model. To illustrate this problem, a comparison was made between the analytical bottom stress and computed bottom stresses from the DSS and the VS over the practical range of K and σ_0. The DSS reproduces bottom stress exactly using two LPs. On the other hand, Table II presents a summary of the number of LPs required for the computed bottom stress using the VS to come within 10% of the analytical bottom stress as a function of K and σ_0. Clearly, it is computationally practical to use the VS only for large roughnesses and large amounts of slip, both of which tend to minimize the velocity gradient at the bottom.

Although quite simple, the steady state case demonstrates the relative ease with which a DSS solution can resolve a realistic boundary layer (i.e. no bottom slip and a linearly varying eddy viscosity) in a hydrodynamic model that explicitly includes the vertical dimension. In the following examples we evaluate how this highly desirable capability is affected by unsteady conditions. Only the no-slip case ($K=1000$) is considered.

Periodic forcing

Assuming a periodic surface stress of the form $\tau_s(t)/\rho=(\tau_s/\rho)e^{i\omega t}$ (where ω is the forcing frequency and $i\equiv\sqrt{(-1)}$), solutions can be sought to equations (1) and (5)–(7) that have the form $\bar{U}(t)=\bar{U}e^{i\omega t}$, $u(\sigma, t)=u(\sigma)e^{i\omega t}$, $\tau_b(t)/\rho=(\tau_b/\rho)e^{i\omega t}$ and $\eta(t)=\eta e^{i\omega t}$. (Note that τ_s/ρ, $\bar{U}$, $u(\sigma)$, τ_b/ρ and η are all complex variables; therefore they may be out of phase with each other.) Substituting these in equations (1) and (5)–(7) transforms the linear hydrodynamic equations into

$$i\omega\eta+h\frac{\partial\bar{U}}{\partial x}=0, \tag{31}$$

$$i\omega\bar{U}=-g\frac{\partial\eta}{\partial x}+\frac{1}{h\rho}(\tau_s-\tau_b), \tag{32}$$

$$i\omega u-\frac{a-b}{h}\frac{\partial}{\partial\sigma}\left[\frac{(a-b)E_z}{h}\frac{\partial u}{\partial\sigma}\right]=\frac{1}{h\rho}(\tau_b-\tau_s). \tag{33}$$

The procedure used to solve equations (31)–(33) analytically together with the linear slip boundary condition has been presented previously[1,16] and is not repeated here. Rather, the solutions are given without derivation in Table III.

Spectral approximations for the periodic case are generated by expressing $\beta_n(t)=\beta_n e^{i\omega t}$ and $\alpha_n(t)=\alpha_n e^{i\omega t}$ and substituting these as well as the periodic forms of $u(t)$, $\tau_z(\sigma, t)/\rho$, $\tau_s(t)/\rho$, $\tau_b(t)/\rho$ and $\bar{U}(t)$ in equations (14)–(16), (21), (22) and (24). The resulting equations are listed in Table IV.

The periodic solution depends on the dimensionless parameters K and σ_0 (as found for the steady state solution), a dimensionless channel length L', a dimensionless frequency Ω and the dimensionless position in the channel, x/L. L' is the ratio of the channel length L to the wave length of a shallow water wave having period ω, equation (38). Ω is the ratio of the time scale for momentum to be transported through the water depth, h^2/E_{z0}, and the forcing time scale $1/\omega$, equation (39). Assuming ranges for ω of 10^{-3}–10^{-5} s^{-1}, L of 1–10^3 km and h and U_b^* as given previously suggests $L'\sim10^{-5}$–10^{2} and $\Omega\sim10^{-4}$–10^{2}. In all cases results are presented for $x/L=0{\cdot}5$ since these are representative of the behaviour throughout the rest of the channel.

Figures 2 and 3 present magnitude and phase portraits of the velocity structure for $K=1000$, $L'=1$ and four combinations of σ_0 and Ω. For the case $\Omega=10^{-1}$ momentum is transported

Table III. Analytical solution for the periodic test case

$$\frac{u(\sigma)E_{z0}}{h\tau_s/\rho}=\frac{U_0E_{z0}}{h\tau_s/\rho}\left[\frac{A_1(\sigma)-\bar{A}_1}{B}\right]+\frac{1}{2(2+\sigma_0)}\left[\frac{A_2(\sigma)-\bar{A}_2}{B}\right], \tag{34}$$

$$\frac{\bar{U}E_{z0}}{h\tau_s/\rho}=\frac{U_0E_{z0}}{h\tau_s/\rho}\left[1+\frac{\bar{A}_1}{B}\right]+\frac{1}{2(2+\sigma_0)}\frac{\bar{A}_2}{B}, \tag{35}$$

$$\frac{\tau(\sigma)}{\tau_s}=\left[2\frac{U_0E_{z0}}{h\tau_s/\rho}\frac{\dot{A}_1(\sigma)}{B}+\frac{1}{2+\sigma_0}\frac{\dot{A}_2(\sigma)}{B}\right](\sigma+1+\sigma_0), \tag{36}$$

$$\frac{U_0E_{z0}}{h\tau_s/\rho}=\frac{i(1+\gamma_2)}{\Omega}\left[\frac{[1-\exp(-\lambda L')]\exp(\lambda L'x/L)-[1-\exp(\lambda L')]\exp(-\lambda L'x/L)}{\exp(\lambda L')-\exp(-\lambda L')}\right], \tag{37}$$

$$L'\equiv\frac{\omega L}{\sqrt{(gh)}}, \tag{38}$$

$$\Omega\equiv\frac{\omega h^2}{E_{z0}}, \tag{39}$$

$$\lambda\equiv\sqrt{(i\gamma_1-1)}, \tag{40}$$

$$\gamma_1\equiv\frac{2\dot{A}_1(-1)}{\Omega(\bar{A}_1+B)}\sigma_0, \tag{41}$$

$$\gamma_2\equiv\left[\frac{\dot{A}_1(-1)\bar{A}_2}{B(\bar{A}_1+B)}-\frac{\dot{A}_2(-1)}{B}\right]\frac{\sigma_0}{2+\sigma_0}, \tag{42}$$

$$A_1(\sigma)\equiv\mu_1(\sigma)\dot{\mu}_2(1)-\mu_2(\sigma)\dot{\mu}_1(1), \tag{43}$$

$$A_2(\sigma)\equiv\mu_1(\sigma)\left[\mu_2(-1)-\frac{2\sigma_0}{K}\dot{\mu}_2(-1)\right]-\mu_2(\sigma)\left[\mu_1(-1)-\frac{2\sigma_0}{K}\dot{\mu}_1(-1)\right], \tag{44}$$

$$B\equiv\dot{\mu}_1(1)\left[\mu_2(-1)-\frac{2\sigma_0}{K}\dot{\mu}_2(-1)\right]-\dot{\mu}_2(1)\left[\mu_1(-1)-\frac{2\sigma_0}{K}\dot{\mu}_1(-1)\right], \tag{45}$$

$$\mu_1(\sigma)=\mathrm{ber}\{[\Omega(\sigma+1+\sigma_0)]^{1/2}\}+i\,\mathrm{bei}\{[\Omega(\sigma+1+\sigma_0)]^{1/2}\}, \tag{46}$$

$$\mu_2(\sigma)=\mathrm{ker}\{[\Omega(\sigma+1+\sigma_0)]^{1/2}\}+i\,\mathrm{kei}\{[\Omega(\sigma+1+\sigma_0)]^{1/2}\}. \tag{47}$$

Ber, bei, ker and kei are zeroth-order Kelvin functions;[19] an overdot $(\dot{})\equiv\partial/\partial\sigma$; an overbar $(\bar{})\equiv\frac{1}{2}\int_{-1}^{1}d\sigma$.

through the depth in only a fraction of the forcing period. Figures 2(a), 2(b) and 3(a), 3(b) show that the velocity magnitude and phase obtained from the DSS using two LPs are virtually identical to the analytical solution and therefore that the stress variation is very close to linear over the depth. This linear stress variation suggests that the momentum balance over the depth is nearly at steady state and is consistent with the low value of Ω. Since steady state is approached as $\Omega\to0$, the DSS using two LPs gives a highly accurate solution for $\Omega<10^{-1}$ as well. The VS is able to capture the phase change through the water column with a comparable number of LPs to the DSS. However, as was the case at steady state, for $\sigma_0=10^{-2}$ approximately 10 LPs and for $\sigma_0=10^{-4}$ more than 20 LPs are required to reproduce the velocity magnitude with an accuracy comparable to the DSS using two LPs.

Table IV. Galerkin–spectral equations for the periodic test case

Velocity expansion

$$u(\sigma) \equiv \sum_{n=1}^{N} \beta_n \phi_n(\sigma), \tag{48}$$

$$m \geqslant 1: \quad \frac{h^2}{4} \sum_{n=1}^{N} \mathrm{i}\omega\beta_n \int_{-1}^{1} \phi_m(\sigma)\phi_n(\sigma)\,\mathrm{d}\sigma + \sum_{n=1}^{N} \beta_n \int_{-1}^{1} E_z(\sigma) \frac{\partial \phi_n(\sigma)}{\partial \sigma} \frac{\partial \phi_m(\sigma)}{\partial \sigma}\,\mathrm{d}\sigma = \frac{h}{2}\left[\frac{\tau_s}{\rho} - \frac{\tau_b}{\rho}\phi_m(-1)\right], \tag{49}$$

$$\sum_{n=1}^{N} \beta_n \phi_n(-1) = -\bar{U} + \frac{\tau_b}{k\rho}. \tag{50}$$

Stress expansion

$$\frac{\tau_z(\sigma)}{\rho} \equiv \sum_{n=0}^{N} \alpha_n \phi_n(\sigma), \tag{51}$$

$$m \geqslant 1: \quad \frac{h^2}{4} \sum_{n=0}^{N} \mathrm{i}\omega\alpha_n \int_{-1}^{1} \phi_m(\sigma) \int_{-1}^{\sigma} \frac{\phi_n(\sigma)}{E_z(\sigma)}\,\mathrm{d}\sigma\,\mathrm{d}\sigma + \sum_{n=0}^{N} \alpha_n \left[\int_{-1}^{1} \phi_n(\sigma) \frac{\partial \phi_m(\sigma)}{\partial \sigma}\,\mathrm{d}\sigma + \phi_n(-1)\,\phi_m(-1)\right] = \frac{\tau_s}{\rho}, \tag{52}$$

$$\sum_{n=0}^{N} \alpha_n \left[\frac{\phi_n(-1)}{kh} + \frac{1}{4}\int_{-1}^{1} \int_{-1}^{\sigma} \frac{\phi_n(\sigma)}{E_z(\sigma)}\,\mathrm{d}\sigma\,\mathrm{d}\sigma\right] = \frac{\bar{U}}{h}. \tag{53}$$

For the case $\Omega = 10$ the vertical momentum balance is no longer near steady state; consequently, the DSS requires more than two LPs to capture the vertical stress variation. Figures 2(c), 2(d) and 3(c), 3(d) suggest that approximately four LPs may be needed by the DSS. The VS, however, requires at least 10 LPs for $\sigma_0 = 10^{-2}$ and more than 20 LPs for $\sigma_0 = 10^{-4}$.

Figures 4 and 5 compare the amplitude and phase behaviour of the analytical solution for bottom stress with solutions obtained using the DSS and VS. These runs were made using a single value of $\sigma_0 = 10^{-3}$ but varying Ω and L'. The 10^4 change in L' has minimal effect in these pictures, indicating that the number of LPs required for the DSS or the VS to converge to the analytical solution is only very weakly dependent on L'. For $\Omega \leqslant 1$ the DSS with two LPs is nearly identical to the analytical solution, while for larger Ω the number of LPs required by the DSS increases to as many as seven for $\Omega = 10^2$. Considering the fact that comparable results using the VS require the use of more than 20 LPs, the DSS is computationally quite superior to the VS for all Ω.

Although the Coriolis force was omitted from these test cases, the results can be used to infer whether a DSS will be equally effective when the Coriolis force is included. The counterparts to equation (33) for the case in which Coriolis is included are

$$\mathrm{i}\omega u_x - f u_y = \frac{a-b}{h}\frac{\partial}{\partial \sigma}\left(\frac{(a-b)E_z}{h}\frac{\partial u_x}{\partial \sigma}\right) + \frac{1}{h\rho}(\tau_{bx} - \tau_{sx}), \tag{54}$$

$$\mathrm{i}\omega u_y + f u_x = \frac{a-b}{h}\frac{\partial}{\partial \sigma}\left(\frac{(a-b)E_z}{h}\frac{\partial u_y}{\partial \sigma}\right) + \frac{1}{h\rho}(\tau_{by} - \tau_{sy}), \tag{55}$$

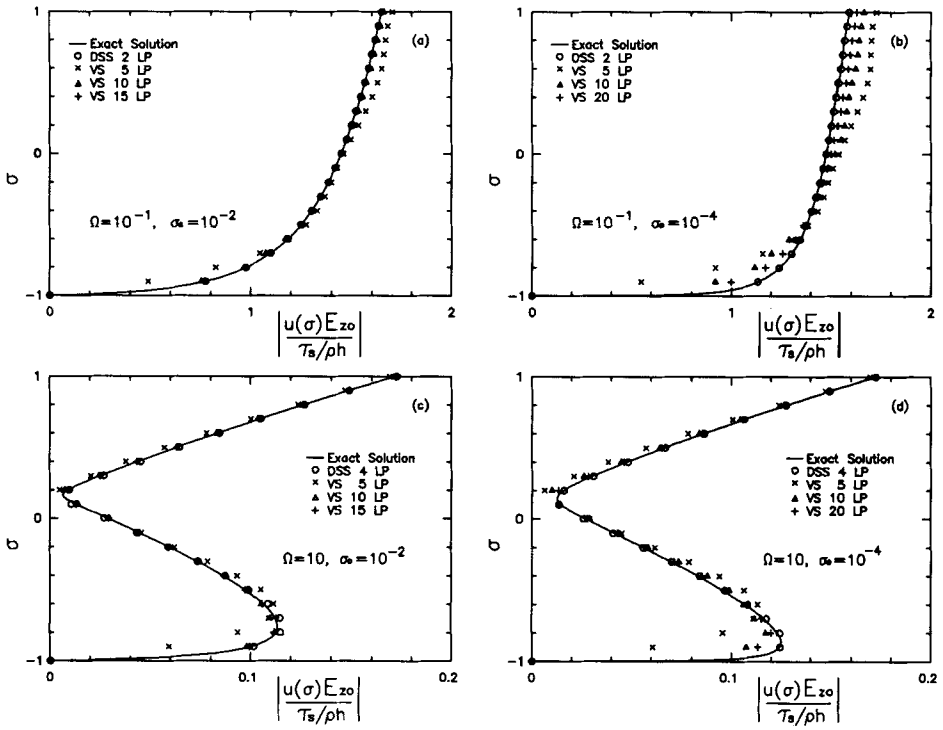

Figure 2. Vertical profiles of horizontal velocity magnitude for the periodic test case

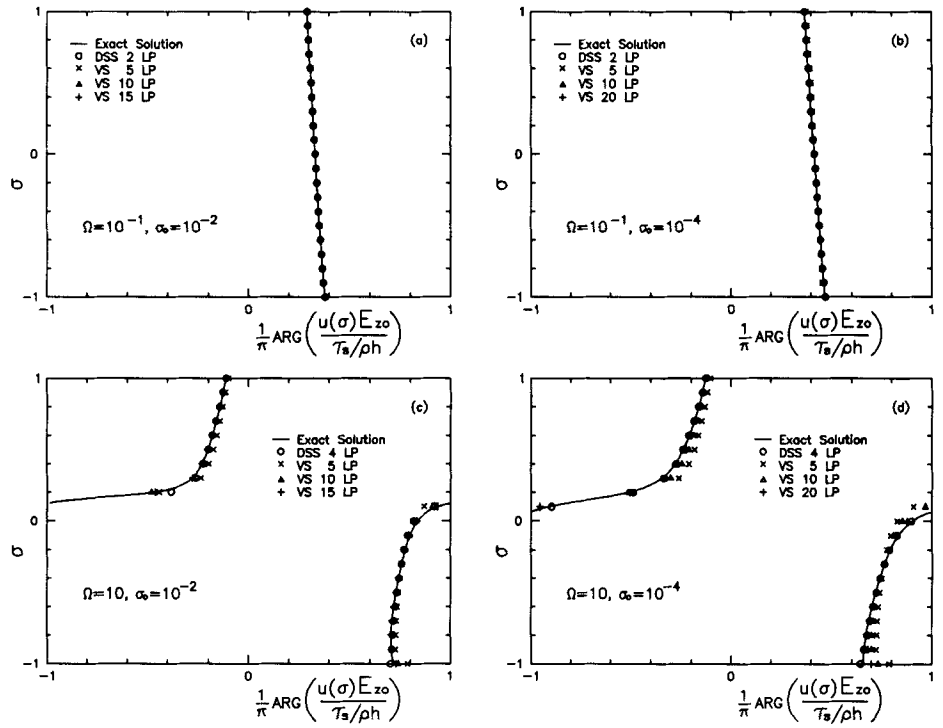

Figure 3. Vertical profiles of horizontal velocity phase for the periodic test case

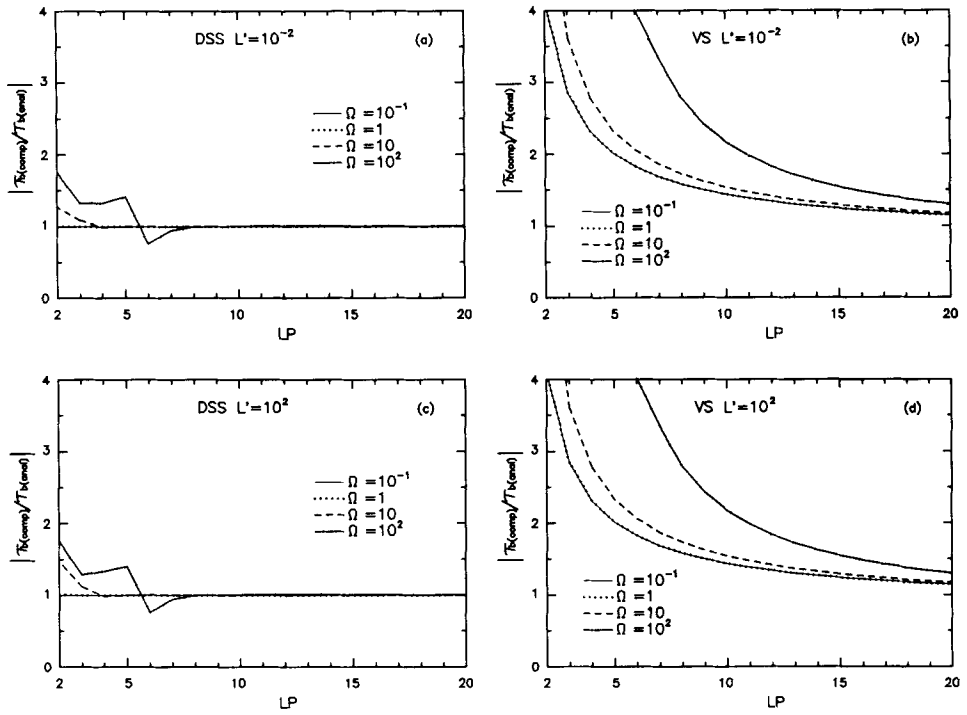

Figure 4. Ratio of spectral to analytical bottom stress magnitude for the periodic test case

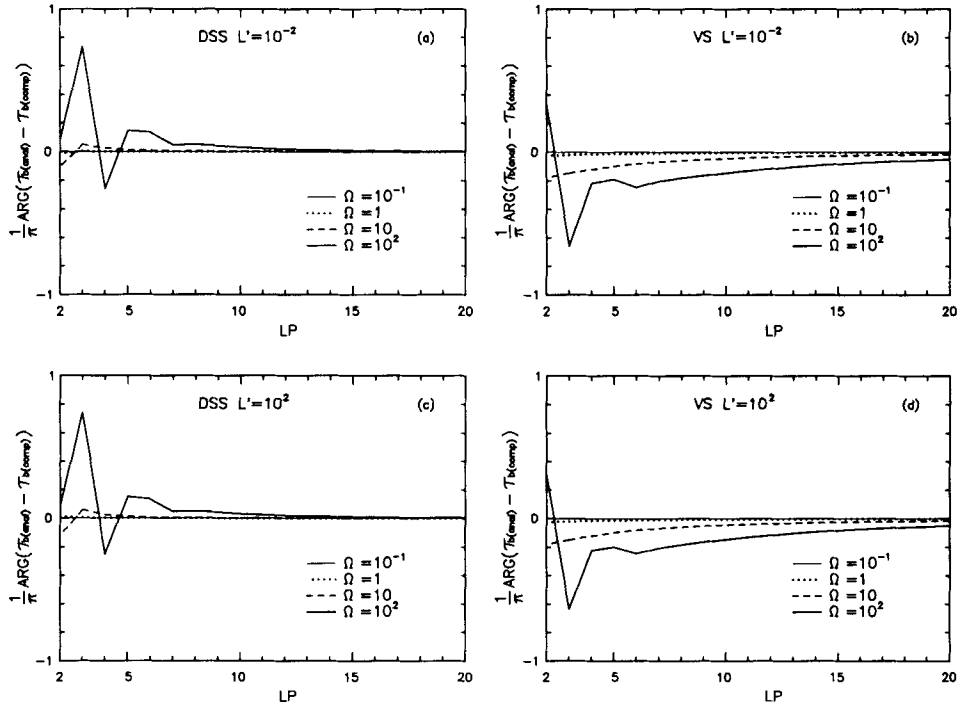

Figure 5. Ratio of spectral to analytical bottom stress phase for the periodic test case

where subscripts x and y have been appended to the velocity and stress terms to indicate components in the two horizontal directions and f is the Coriolis parameter. It has been shown[1] that the linear combinations of u_x and u_y

$$v^+ \equiv \frac{u_x + iu_y}{2} \quad \text{and} \quad v^- \equiv \frac{u_x - iu_y}{2}$$

transform equations (54) and (55) into

$$i(\omega+f)v^+ - \frac{a-b}{h}\frac{\partial}{\partial\sigma}\left(\frac{(a-b)E_z}{h}\frac{\partial v^+}{\partial\sigma}\right) = \frac{1}{2h\rho}[(\tau_{bx}-\tau_{sx})+i(\tau_{by}-\tau_{sy})], \tag{56}$$

$$i(\omega-f)v^- - \frac{a-b}{h}\frac{\partial}{\partial\sigma}\left(\frac{(a-b)E_z}{h}\frac{\partial v^-}{\partial\sigma}\right) = \frac{1}{2h\rho}[(\tau_{bx}-\tau_{sx})-i(\tau_{by}-\tau_{sy})]. \tag{57}$$

Equations (56) and (57) show that the vertical structures of v^+ and v^- are uncoupled and that each is analogous to the structure of u in the absence of the Coriolis force, except that v^+ is forced by the frequency $\omega+f$ and v^- is forced by the frequency $\omega-f$. Therefore we expect that the vertical structures of v^+ and v^- will depend on the dimensionless frequencies $\Omega^+ \equiv \Omega + \mathscr{F}$ and $\Omega^- \equiv \Omega - \mathscr{F}$ respectively, where $\mathscr{F} \equiv fh^2/E_{z0}$. At mid latitudes $f \sim 10^{-4}\ s^{-1}$, giving the range of $\mathscr{F} \sim 10^{-3}$–10. This yields values for Ω^+ and Ω^- in the same range as Ω; consequently, the results shown in Figures 2–5 are also indicative of the performance of the DSS and the VS when the Coriolis force is included in the governing equations.

Transient forcing

Analytical solutions can be obtained to equations (1) and (5)–(7) for a transient forcing by decomposing the forcing into its Fourier components, using the periodic solutions presented in Table III for each Fourier component and superimposing the resulting periodic solutions. In this subsection an illustrative set of results for bottom stress are presented for the often-used problem of an instantaneously imposed wind on an initially quiescent channel. Representative values of $L = 100$ km, $h = 50$ m, $\sigma_0 = 0{\cdot}01$ and $E_{z0} = 0{\cdot}5\ m^2\ s^{-1}$ are used.

An instantaneously imposed forcing cannot be represented exactly by a finite Fourier series; however,

$$\frac{\tau_s(t)}{\tau_{s-steady}} = \frac{1}{2} + 2\sum_{n=1}^{N}\frac{\sin[(2n-1)\pi t/T]}{\pi(2n-1)} \tag{58}$$

gives an approximation to a square wave of period T, as shown in Figure 6. By selecting T to be

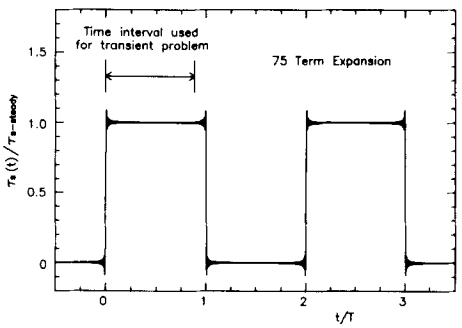

Figure 6. Fourier series approximation to a square wave (equation (58)) used to represent an instantaneously applied wind for the transient test case

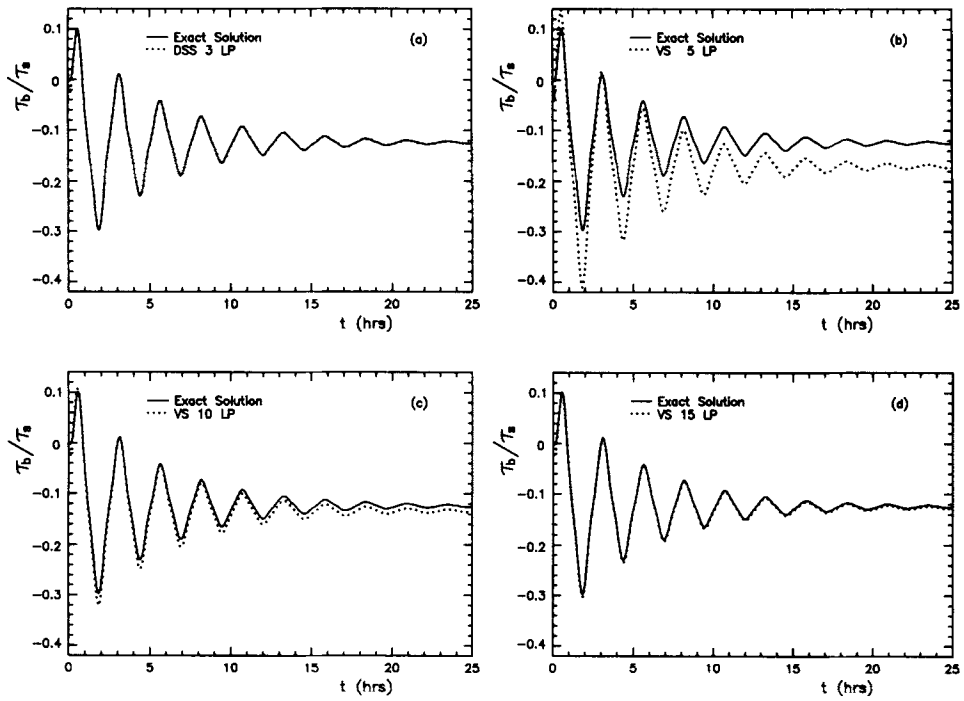

Figure 7. Time histories of bottom stress for the transient test case

much larger than the time required for the basin to reach steady state and considering only the period $0 \leqslant t/T < 1$, a reasonable representation of an instantaneously imposed wind can be obtained and used to develop an approximate analytical solution. Sensitivity analyses indicated that when 50 or more terms were used in equation (58), minimal change occurred in the analytical solution of the basin response and any change that did occur was limited to times very close to zero (i.e. of the order of $t/T < 1\%$). Seventy-five terms ($N = 74$) were used in equation (58) for the solution shown in Figure 6 and the runs presented below.

The VS and the DSS for the transient test case were obtained by discretizing equations (15) and (22) in time using a Crank–Nicholson scheme. As discussed above, the analytical solution for $\bar{U}$ was used to force these equations, thereby eliminating any feedback of error from the vertical representation into $\bar{U}$. Figure 7 presents a comparison between bottom stresses obtained analytically and from the VS and the DSS. The DSS with three LPs is quite close to the analytical solution except very near $t = 0$ (due primarily to the overshoot in the forcing in Figure 6). Conversely, 15 or more LPs are required for the VS to attain comparable accuracy. We note that this test case uses σ_0 at the upper limit of the practical range and therefore is the easiest case for the VS to capture. For smaller values of σ_0 the transient performance of the VS becomes even poorer, as suggested by the steady state results in Table II.

CONCLUSIONS

A simple technique has been presented that allows a numerical solution to be sought for the vertical variation of shear stress as a substitute for the vertical variation of velocity in a three-dimensional hydrodynamic model. The rationale for preferring a solution for shear stress to one

for velocity is that shear stress tends to vary more slowly over the vertical than velocity, particularly near boundaries.

In its most general form the DSS technique depends only on the validity of an eddy viscosity relation between the shear stress and the vertical gradient of velocity. The equations that must be solved to use the DSS technique contain both integral and differential terms; therefore it is convenient to use a discretization over the vertical that expresses stress in terms of assumed shape functions. Depending on the choice of shape functions and the functional variation of eddy viscosity over the depth, the velocity profile can be recovered from the stress profile by solving equation (4) in closed form. Under these conditions the difficulties associated with numerically integrating a near-logarithmic singularity are avoided. Most practical problems can be solved subject to this restriction by allowing a global or piecewise polynomial variation of τ_z and a piecewise linear variation of E_z.

Using the Galerkin–spectral method with Legendre polynomials to discretize over the vertical, solutions obtained using the DSS and the VS techniques were compared with analytical solutions for the test case of wind-driven circulation in an unstratified, closed, rectangular channel governed by the linear equations of motion. When the forcing time scale had an order of magnitude equal to or longer than the time scale for momentum transport over the depth ($\Omega \leqslant 1$), a DSS using an expansion of only two LPs gave nearly exact results. For higher-frequency forcing or a slower vertical momentum transport rate the DSS required more LPs; however, for most practical cases the computational effort remained very reasonable. In no case was the computational effort required by the VS remotely competitive with the DSS when a physically realistic boundary layer was included. This result is made even more significant by the fact that the eddy viscosity used here favoured the VS because it produced only a single boundary layer at the bottom rather than a boundary layer at the bottom and at the free surface. Had both boundary layers been included, the computational effort associated with the VS would have been substantially greater while the effort needed for the DSS would have remained essentially the same.

The DSS technique has been formulated for the linearized governing equations considered here by solving a two-dimensional problem for the depth-averaged velocity and a one-dimensional problem for the vertical distribution of shear stress. A directly analogous procedure can be used for the non-linear problem if the convective terms are neglected in the equations for the vertical variation of momentum.[3,9] In this case the vertical problem can be solved locally using the DSS at each horizontal grid point. The computed bottom stress and the shear dispersion terms can then be fed into the non-linear equations for the depth-averaged velocity to complete the solution. Because the vertical problem is computed locally, the coarseness of the discretization used for the DSS can vary horizontally, depending on the ratio of the forcing time scale to the momentum transport time scale (e.g. Ω). This approach can be extended to the fully non-linear, three-dimensional equations for nearly horizontal flow by treating the convective terms in the DSS equations for the vertical variation of momentum explicitly[18] or iteratively.[3]

Our experience using the DSS with the Galerkin–spectral expansion for the linearized governing equations suggests that for realistic, unstratified, coastal applications with relatively simple eddy viscosity profiles, highly accurate transient solutions should require only three to four LPs. In practical applications in which E_z varies in time, the N^3 computational burden associated with the Galerkin–spectral method is of little consequence for very low numbers of LPs (e.g. $N \leqslant 5$). However, this changes rapidly as the number of LPs increases. We are presently investigating the use of the finite element method with linear bases to discretize the DSS equations over the vertical. Preliminary results seem quite promising because the problem can be arranged to give a tridiagonal system of equations and consequently a highly efficient numerical

solution for even a large number of elements. Also, the closed-form solution of equation (4) is simplified and the element sizes can be adjusted to achieve an Ω (based on the element size rather than the entire depth) that allows the stress to be represented accurately by a linear function across the element. Alternatively, the element could be selected to match the computational grid for E_z if a higher-order closure model is used.

The DSS technique should be quite beneficial in modelling relatively shallow water bodies in which the bottom and surface boundary layers, or velocity gradients generated across sharp density interfaces, occupy a significant portion of the water depth.

ACKNOWLEDGEMENTS

This work was supported by the U.S. Army Corps of Engineers Waterways Experiment Station Dredging Research Program under contract DACW39-86-D-004/0001.

REFERENCES

1. D. R. Lynch and C. B. Officer, 'Analytic test cases for three-dimensional hydrodynamic models', *Int. j. numer. methods fluids*, **5**, 529–543 (1985).
2. H. L. Jenter and O. S. Madsen, 'Bottom stress in wind-driven depth-averaged coastal flows', *J. Phys. Oceanogr.*, **19**, 962–974 (1989)
3. J. J. Nihoul and S. Djenidi, 'Perspective in three-dimensional modelling of the marine system', in J. J. Nihoul and B. M. Jamart (eds), *Three-dimensional Models of Marine and Estuarine Dynamics*, Elsevier, Amsterdam, 1987, pp. 1–19.
4. A. F. Blumberg and G. L. Mellor, 'A description of a three-dimensional coastal ocean circulation model', in N. S. Heaps (ed.), *Three-dimensional Coastal Ocean Models*, AGU Press, Washington, DC, 1987, pp. 1–16.
5. A. M. Davies, 'On formulating two-dimensional vertically integrated hydrodynamic numerical models with enhanced representation of bed stress', *J. Geophys. Res.*, **93**, 1241–1263 (1988).
6. A. Monin and A. Yaglom, *Statistical Hydromechanics, Vol. 1*, MIT Press, Cambridge, Ma, 1971.
7. H. Schlichting, *Boundary Layer Theory*, 7th edn, McGraw-Hill, New York, 1979.
8. W. D. Grant and O. S. Madsen, 'The continental shelf bottom boundary layer', *Ann. Rev. Fluid Mech.*, **18**, 265–305 (1986).
9. A. M. Davies, 'Spectral models in continental shelf oceanography', in N. S. Heaps (ed.), *Three-dimensional Coastal Ocean Models*, AGU Press, Washington, DC, 1987, pp. 71–106.
10. W. Rodi, 'Examples of calculation methods for flow and mixing in stratified fluids', *J. Geophys. Res.*, **92**, 5305–5328 (1987).
11. W. Rodi, *Turbulence Models and their Aplication in Hydraulics*, International Association for Hydraulic Research, Delft, 1980.
12. M. B. Abbott, 'Numerical modeling of free surface flows that are two-dimensional in plan', in H. B. Fischer (ed.), *Transport Models for Inland and Coastal Waters*, Academic Press, New York, 1981, pp. 222–283.
13. J. K. Lee and D. C. Froehlich, 'Review of the literature on the finite-element solutions of the equations of two-dimensional surface-water flow in the horizontal plane', *Open-File Report 85-96*, U.S. Geological Survey, Reston, VA, 1985.
14. G. Furnes, 'A three-dimensional numerical sea model with eddy viscosity varying piecewise linearly in the vertical', *Continental Shelf Res.*, **2**, 231–241 (1983).
15. A. M. Davies and A. Owen, 'Three-dimensional numerical sea model using the Galerkin method with a polynomial basis set', *Appl. Math. Modelling*, **3**, 421–428 (1979).
16. A. M. Davies and C. V. Stephens, 'Comparison of finite difference and Galerkin methods as applied to the solution of the hydrodynamic equations', *Appl. Math. Modelling*, **7**, 226–239 (1983).
17. P. M. Gresho, R. L. Lee and R. L. Sani, 'The consistent method for computing derived boundary quantities when the Galerkin FEM is used to solve thermal and/or fluids problems', *Int. j. numer. methods fluids*, **7**, 371–394 (1987).
18. D. R. Lynch and F. E. Werner, 'Three-dimensional hydrodynamics on finite elements. Part II: Non-linear time-stepping model', *Int. j. numer. methods fluids*, **12**, 507–533 (1991).
19. M. Abramowitz and I. A. Stegun, *Handbook of Mathematical Functions*, 9th edn, Dover, New York, 1972.